ACS OMEGA

Open Access

http://pubs.acs.org/journal/acsodf

Article

Dissipative Particle Dynamics Using Conductor-Like Screening Model for Real Solvents-Based Interaction Parameters for Classical Simulations of Dibenzothiophene Adsorption on Molybdenum Disulfide Nanoparticles

Estela Mayoral, Ivonne Judith Hernández-Hernández, José-Manuel Martínez-Magadán, Jaime Klapp,* Carolina Zuriaga-Monroy, Miriam Ballesteros-Olvera, and Raúl Oviedo-Roa*

Cite This: *ACS Omega* 2024, 9, 45706−45718

Read Online

ACCESS | Metrics & More | Article Recommendations

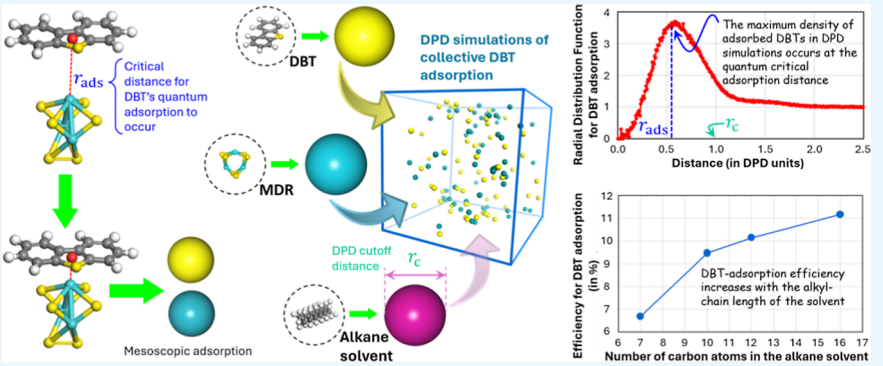

ABSTRACT: The previous step before the catalytic activity of MoS_2 nanoparticles for the hydrodesulfurization of dibenzothiophene (DBT), i.e., the DBT adsorption, is studied through dissipative-particle-dynamics (DPD) simulations. Density-functional-theory (DFT) calculations reveal that although DBT is chemisorbed, and, therefore, there is an intermolecular electronic exchange leading to the weakening of the DBT's C−S bonds, the formed individual linking bonds among DBT and MoS_2 are noncovalent, fact that allows the application of DPD in order to at least qualitatively estimate the fraction of the content of DBT molecules within an oleic solvent that can be adsorbed by the MoS_2 nanoparticles. With the sake of getting realistic insights, we calculated the classical-DPD interaction parameters through the quantum-statistical approach conductor-like screening model for real solvents. A comparison between DFT calculations and the DPD simulations reveals that the quantum spontaneous attraction of DBT by MoS_2 nanoparticles begins at the distance where the DBT's volumetric density in the neighborhood of a MoS_2 nanoparticle is maximum, as well as that the alkylic chain of the oleic solvent has an important influence on the performance of the catalyst since the chain length increases the probability that DBT will find MoS_2. These results suggest the combined DFT and DPD study can be useful for the design of HDS catalysts.

1. INTRODUCTION

Considerable contents of asphaltenes in heavy crude oil increase its viscosity, making difficult its extraction, storage, transportation, and processing.[1] Asphaltenes are polynuclear aromatic sheets characterized by hexagonal carbon rings. They can contain different proportions of heteroatoms, mainly oxygen, nitrogen, and sulfur, which significantly drive the initial attraction among asphaltenes leading to asphaltenic layers and reducing, therefore, the oil recovery through plugging of rock pores as well as of equipment.[2] Asphaltenes cause problems such as deposition in lines and diminution of the production of distillable products in oil refining due to their high resistance to disintegration. For this reason, they are initiators and motivators of coke formation in catalytic processes, causing significant deactivation of catalysts,[3] aggravated by the metals present in the crude oil, more than 90% of which are found in the asphaltenic fraction.[4]

Owing to the above disadvantages in the production and processing of heavy crude oil, asphaltenes are considered the

Received: December 1, 2023
Revised: June 4, 2024
Accepted: June 6, 2024
Published: November 4, 2024

lowest value components, and then alternatives have been investigated to eliminate or reduce them before crude oil enters into the refining process. However, the tendency to produce and refine heavy crude oil is increasing,[5] making essential to conduct fundamental research about asphaltenes relying on the molecular and mesoscopic computational modeling. At this respect, it is worthy to mention that classical and quantum theoretical methods, computer speed, computer memory, and algorithms efficiency have been used to model and improve physical and chemical processes, allowing the wide applications of molecular modeling to numerous fields like hydrotreatment of the crude oil.[6]

An important step in the heavy-oil refinement process is the hydrodesulfurization (HDS), which is a chemical reaction, usually triggered by Ni or Co-doped catalysts containing molybdenum or wolfram, aimed at removing sulfur impurities. The HDS process consists basically of two procedures: desulfurization and hydrogenation. In desulfurization, it occurs breaking of the C−S bonds inside the sulfur-containing compounds, whereas in hydrogenation, molecular hydrogen reacts with sulfur releasing H_2S from the now sulfur-free hydrocarbons.[7] The selectivity and activity of HDS depend on the nature of the oil fraction, the type of the catalyst, the concentration of active sites, and the reaction conditions of pressure and temperature.[2,6−11]

Approximate molecular structures for heavy crude oil's asphaltenes and resins have been proposed,[8,9,12] it being thiophene and dibenzothiophene, some of the compounds most widely used for modeling HDS of fuels.[7,13,14] The initial adsorption of sulfur-containing molecules on the catalysts' active sites is an important stage of the HDS process. The interaction of thiophene on the catalytically active surfaces of MoS_2 has been theoretically studied through the extended-Hückel tight-binding method, molecular-orbital techniques, and ab initio density-functional-density (DFT) approximations.[6,7,14−21] It is worthy to mention that the MoS_2 catalyst belongs to the general family of two-dimensional metal dichalcogenides materials (e.g., WS_2, $MoSe_2$, WSe_2, $MoTe_2$, etc.), some of which have been theoretically studied through van der Waals-corrected DFT to be used alone in a pristine or doped (e.g., with N, Al, P, or Si) form, or in nanocomposites (e.g., with TiO_2) for adsorption of molecules (e.g., CO, NO, O_3, SO_2, and SO_3).[22−25]

In a hydrotreating reactor, the catalysts are in contact with a hydrocarbon flow; therefore, the efficiency of the hydroprocessing is related to the fraction of sulfur-containing hydrocarbons that are adsorbed by the catalysts. The collective adsorption of sulfur-containing hydrocarbons can be classically simulated by performing mesoscopic dynamics, i.e., on a scale in which the molecules are not modeled at the atomistic level but instead at the granular one in which a grain, or bead as it is called, represents several atoms or functional groups of a portion of a molecule.[13] Mesoscopic simulations can be performed through the dissipative-particle-dynamics (DPD) approach, which requires the estimation of the so-named interaction parameters between pairs of beads from the chemical information on the interacting molecules.

Whereas elsewhere in the literature the computational study of the adsorption of single sulfur-containing molecules on MoS_2 surfaces and nanoparticles has been reported,[18] at this work quantum interactions among dibenzothiophene (DBT) and the MoS_2 catalyst have been mapped onto the mesoscale by using a quantum-statistical method reported in ref 26, and applied to perform DPD simulations for the sake of theoretical modeling of the collective adsorption of DBT by MoS_2; the theoretical methodology shown herein could help to design better catalysts.

We began with the building and quantum validation of atomistic molecular structures to model the step prior to hydrotreating, that is, the adsorption of a single sulfur-containing hydrocarbon by the catalyst, leading to a weakening of the S−C covalent bonds that can be broken in subsequent catalytic reactions. Next, from the atomistic molecular structures, we built mesoscopic beads for modeling the catalyst, the sulfur-containing hydrocarbon, and the solvents within which both the sulfur-containing hydrocarbon and the catalyst are dissolved, and mapped the quantum intermolecular information toward these mesoscopic beads. The methodology for this quantum-to-mesoscopic mapping consists of the computation by means of quantum statistical thermodynamics of infinite-dilution activity coefficients, which are used as input parameters to calculate the interaction among beads required by DPD simulations.[26] In this way, it is guaranteed that the mesoscopic scale contains proper information from the atomistic molecular models. Finally, we performed DPD runs on solutions containing catalysts and hydrocarbons.

2. THEORETICAL METHODOLOGY

We use the DBT molecule (Figure 1a) as the sulfur-containing molecule model because it is a common moiety of the asphaltane aromatic sheets. Likewise, for the HDS catalyst we use a Mo_3S_6 single hexagonal ring (MDR, Figure 1c) as the simplest model preserving the MoS_2 topology consisting of molybdenum atoms connected to each other by pairs of sulfur atoms, just as they connect on the crystalline network. The MDR model exposes unsaturated Mo atoms, which are known reaction sites for the catalytic activity;[14] thus, this model must be sufficient for representing a HDS catalyst. Moreover, this nanoring keeps the Mo:S atomic ratio of the MoS_2 stoichiometry maintaining, therefore, the charges neutrality, and its size is similar to that of DBT, which is a convenient fact for building DPD beads of equal volumes. The chemical

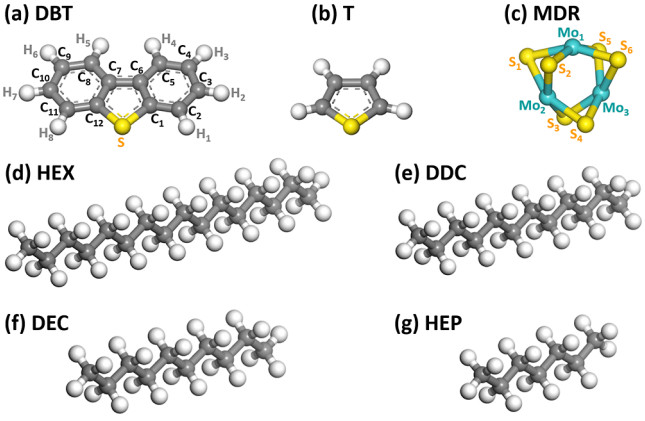

Figure 1. Atomistic models for (a) dibenzothiophene (DBT), (b) thiophene (T), (c) molybdenum-disulfide ring (MDR), (d) *n*-hexadecane (HEX), (e) *n*-dodecane (DDC), (f) *n*-decane (DEC), and (g) *n*-heptane (HEP). Thiophene is a simple molecule used herein to provide quantum insights for the adsorption of its related molecule dibenzothiophene. Atoms' colors denote carbon (gray), hydrogen (white), sulfur (yellow), and molybdenum (cyan).

https://doi.org/10.1021/acsomega.3c09613
ACS Omega 2024, 9, 45706−45718

stability of MDR can be estimated through the thermodynamic formation energy E_F defined herein as[27]

$$E_F = E_{MDR} - 3(E_{Mo} + 2E_S) \quad (1)$$

where E_{MDR} is the energy of MDR, whereas E_{Mo} and E_S are the energy of the single free atoms Mo and S, respectively.

Lastly, since alkylic molecules can be used as model for oil containing sulfur organic molecules,[28] the solvent was modeled through any of the following four molecules: *n*-hexadecane (HEX, Figure 1d), *n*-dodecane (DDC, Figure 1e), *n*-decane (DEC, Figure 1f) and *n*-heptane (HEP, Figure 1g).

2.1. Quantum Modeling. In order to validate that the DBT and MDR molecular models can be used for the mesoscopic simulations, i.e., the binding among them be sufficiently weak to keep their identity, as it happens in classical simulations, we begin by studying the adsorption of DBT by MDR at the quantum level. This validation will also reveal if the minimum small MoS_2-catalyst model MDR has sufficient electronic properties to drive the HDS functionality. Namely, we seek to confirm both the noncovalent nature of the new formed individual bonds in the DBT binding by MDR and the weakening of the DBT's S−C bonds.

To determine the optimal adsorption position of the DBT on MDR, we calculated the highest occupied molecular orbital (HOMO) and the lowest unoccupied molecular orbital (LUMO) for MDR and for the simplest aromatic organosulfur compound, thiophene (T, Figure 1b), which is closely related to DBT and therefore has similar adsorption trends. In basic terms, the chemical reaction between two molecules occurs because the electrons in the HOMO of one molecule are transferred to the LUMO of the other molecule, or vice versa, it being the most viable way the one in which the energetic difference $\Delta E_{H\text{-}L}$ between these intermolecular electronic states is either the smallest for $\Delta E_{H\text{-}L} > 0$ or the most negative for $\Delta E_{H\text{-}L} < 0$; consequently, the best relative molecular orientation triggering the chemical reaction is that where the lobes of the most viable states HOMO and LUMO having the same phase signs overlap in space.

After the molecular models T and MDR are brought near each other according to the topologic criteria described above, the geometry of the resulting complex T:MDR is DFT optimized. Then, we attached benzene rings to the thiophenic ring to complete the model of DBT adsorbed on the MDR, labeled as DBT:MDR, and a subsequent DFT geometric optimization is performed.

The interaction energy ΔE among DBT and MDR is calculated as

$$\Delta E \equiv E_{DBT:MDR} - (E_{DBT} + E_{MDR}) \quad (2)$$

where $E_{DBT:MDR}$ is the energy of the complex DBT:MDR, whereas E_{DBT} and E_{MDR} are the energy of single isolated molecules DBT and MDR, respectively. Each one of these energy values, as well as of those in eq 1, is the total energy E thrown by DFT geometric optimizations, performed through the Materials Studio (MS) DMol^3 software[29] by using the GGA/PBE functional,[30] fine quality for self-consistent-field (SCF) and geometric-optimization convergences, all electrons for the core treatment,[31] thermal occupation of 5×10^{-3} Ha, the double-numerical-plus-polarization (DNP) basis,[32] a global orbital cutoff of 4.9 Å, and the Grimme method for dispersion corrections. The spins were taken as restricted, except for the single isolated atoms Mo and S in eq 1, whose initial spins were taken as the formal ones 6 and 2 (in number of spin unpaired electrons), respectively.

It is worthy to mention that the total electronic energy E calculated through DFT can be broken down as[33]

$$E = E_{non\text{-}dispersion} + E_{dispersion} \quad (3)$$

where the term $E_{non\text{-}dispersion}$ comes from the quantum nature of electrons, i.e., in addition to electrostatic contributions, it has contributions from kinetic, exchange-correlation, and spin polarization; in contrast, the term $E_{dispersion}$ is the long-range dispersion energy, that is, that part of the total electronic energy coming from noncovalent bonds, such as hydrogen bonding and van der Waals interactions. From eq 3, the energy change ΔE of eq 2 can also be expressed as

$$\Delta E = \Delta E_{non\text{-}dispersion} + \Delta E_{dispersion} \quad (4)$$

Therefore, the fractional contributions of $\Delta E_{non\text{-}dispersion}$ and $\Delta E_{dispersion}$ to ΔE provide a natural measure for the chemisorption D_{chem} and physisorption D_{phys} degrees of the adsorption[33]

$$\begin{cases} D_{chem} \equiv \dfrac{\Delta E_{non\text{-}dispersion}}{\Delta E} \\ D_{phys} \equiv \dfrac{\Delta E_{dispersion}}{\Delta E} \end{cases} \quad (5)$$

Likewise, details of the adsorption can be studied by estimating the strength of the bonds formed between the DBT and MDR molecules through the Mayer bond order (MBO), which uses the charge-density bond-order matrix defined from the expansion coefficients of the molecular orbitals. The MBOs values are very close to the corresponding classical chemical bonds, e.g., a double bond has a MBO near 2.0, whereas noncovalent bonds have MBO values near zero or zero.

As a result of the chemisorption contribution to the interaction energy, there must be an exchange of atomic charges Δq_n between DBT and MDR, which we determined through Mulliken charges on the atom n before ($q_{before,n}$) and after ($q_{after,n}$) the adsorption process:

$$\Delta q_n \equiv q_{after,n} - q_{before,n} \quad (6)$$

Positive and negative values of Δq_n indicate that the n-th atom has lost and gained electrons, respectively.

After DBT adsorption, the net charge differences Δq_{DBT} and Δq_{MDR} suffered by DBT and MDR, respectively, are

$$\begin{cases} \Delta q_{DBT} = \displaystyle\sum_{atom_n \in DBT} \Delta q_n \\ \Delta q_{MDR} = \displaystyle\sum_{atom_n \in MDR} \Delta q_n \end{cases} \quad (7)$$

It is to be noted that because the charges are transferred among DBT and MDR, the equality $\Delta q_{MDR} = -\Delta q_{DBT}$ must be accomplished.

The charge redistribution can be analyzed through the charge density difference (CDD), which is a three-dimensional property calculated through the deformation-density DMol^3 task and is defined as the difference between the total density and the density of isolated atoms. Positive and negative values of CDD (i.e., increase and loss of electrical charge densities) indicate depletion and accumulation of electrons, respectively.

https://doi.org/10.1021/acsomega.3c09613
ACS Omega 2024, 9, 45706−45718

Likewise, this analysis is reinforced through the partial density of states.

2.2. Classical Mesoscopic Dynamics. For the mesoscopic dynamics simulations, we represented each of the molecular structures belonging to DBT, MDR, and solvents through corresponding single beads (Figure 2), whose relative

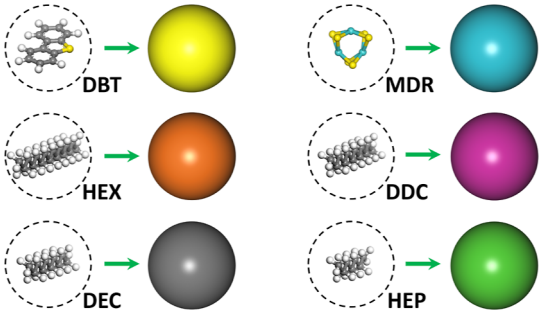

Figure 2. Mapping of the poliatomic molecules shown at Figure 1 onto single beads.

movements were determined herein by solving the Newton's equations under the DPD approximation.[34−36] DPD bead-based simulations allow working with very large amounts of interacting molecules since the single-bead representation of a group of atoms considerably reduces the total number of freedom degrees.

Under the DPD approach, any two beads i and j interact among them through three forces: a conservative one, a dissipative one, and a random one. The dissipative and random forces are linked with each other through the fluctuation-dissipation theorem, producing an integrated thermostat.[35] For its part, the conservative force $\vec{F}_{C_{ij}}$ embodies the essential chemical behavior of the system and consists of a soft repulsion between the beads, given by the following expression

$$\vec{F}_{C_{ij}} = \begin{cases} a_{ij}\left(1 - \frac{r_{ij}}{r_c}\right)\hat{r}_{ij} & \text{if } r_{ij} \le r_c \\ 0 & \text{otherwise} \end{cases} \quad (8)$$

where $\hat{r}_{ij}$ is the unitary vector pointing from the bead i to the bead j, r_{ij} is the relative distance between them, r_c is the cuttoff distance, and the parameter a_{ij}, known as the DPD interaction parameter, is the maximum magnitude of the repulsive force. It is worthy to mention that r_c is taken as the natural unit for lengths; that is, in DPD units, $r_c = 1$. Likewise, since two spherical beads begin to interact among them when they touch each other, their diameters are the same as r_c, independently of the species which they represent to.

For DPD simulation cells having a density ρ of 3 beads per r_c^3 volume, the parameter a_{ij} can be calculated from the Flory-Huggins thermodynamic interaction parameter χ_{ij} of a lab mixture of the molecular substances represented by the beads i and j as[36]

$$a_{ij} = 25 + 3.5\chi_{ij} \quad (9)$$

Physically, χ_{ij} is defined as a dimensionless quantity that characterizes the enthalpy per mol per thermal energy of the mixing process among substances i and j, and it can be calculated for liquids in the molecular level from the activity coefficient at the limit of infinite dilution γ_{ij}^{∞} of the solvent i in the solute j as[26]

$$\chi_{ij}^{\infty} = \ln(\gamma_{ij}^{\infty}) + \ln(v_{ij}) - \left(1 - \frac{1}{v_{ij}}\right) \quad (10)$$

where $v_{ij} = V_j/V_i \ge 1$ is the ratio of the molecular volume V_j of the solute to that V_i of the solvent.

The value of $\ln(\gamma_{ij}^{\infty})$ required at eq 10 can be obtained from the conductor-like screening model (COSMO) for real solvents (RS),[37,38] which is a quantum statistical thermodynamics approach based on screening charges densities (SCDs) over the surfaces of cavities containing molecules in a dielectric medium. The volumes of these cavities coincide quite well with the molecular volumes determined through experimental density,[38] so they were taken as the molecular volumes V_i and V_j for the evaluation of the ratios v_{ij}.

In this paper, we define the volume V_b of a bead as the average of the volumes of the solutes, i.e.,

$$V_b = \frac{1}{2}(V_{DBT} + V_{MDR}) \quad (11)$$

where V_{DBT} and V_{MDR} are the COSMO volumes of DBT and MDR, respectively. Hence, the cuttoff distance r_c can be calculated as[26]

$$r_c = \sqrt[3]{\rho V_b} \quad (12)$$

The liquid mixture of substances i and j is considered by COSMO-RS as a statistical-thermodynamics ensemble of closely packed molecules interacting electrostatically due to the contact of different surface segments, which have a probability $P(\sigma) \equiv p(\sigma)d\sigma$ to have a specific SCD (shortly denoted as σ) within the interval $d\sigma$, where the probability per SCD, $p(\sigma)$, is the so-named σ profile.

2.3. Transference of Quantum Information to the Mesoscopic Scale. We have calculated the DPD interaction parameter a_{ij} by following the steps described below:[26]

(1) The geometry of a molecule is DFT optimized under the COSMO model by using the TURBOMOLE software,[39] which automatically throws molecule's both volume and σ profile at the run's end.

(2) The infinite-dilution activity coefficient γ_{ij}^{∞} is calculated from the σ profiles of molecules i and j by using the COSMO-RS-based COSMOTherm software. For the calculation of the COSMO-volume ratio v_{ij} among a pair of beads, the smaller and greater volumes of the bead-represented molecules are taken as V_i and V_j, respectively.

(3) The Flory-Huggins interaction parameter χ_{ij}^{∞} is obtained by substituting γ_{ij}^{∞} and the COSMO-volumes ratios v_{ij} in eq 10.

(4) Finally, the DPD interaction parameter a_{ij} is calculated through eq 9 for each one of the nine herein-possible binary condensed-phase molecular mixtures, namely, the mixes MDR/DBT, HEX/MDR, HEX/DBT, DDC/DBT, DDC/MDR, MDR/DEC, DEC/DBT, MDR/HEP, and DBT/HEP. For interacting beads of the same species (i.e., $i = j$), eq 9 leads to $a_{ii} = 25$ since they have no mixing heat ($\chi_{ii} = 0$).[26]

The quantum chemical DFT TURBOMOLE runs used the def-TZVP basis set and Becke−Perdew (BP86, i.e., B88-VWN-P86) functional, the DFT-D3 BJ-damping dispersion correc-

https://doi.org/10.1021/acsomega.3c09613
ACS Omega 2024, 9, 45706−45718

tion, restricted spins, infinity dielectric constant, 10^{-6} Ha energy tolerance for SCF convergence, and 10^{-6} Ha energy and 10^{-3} Ha/Bohr force-magnitude tolerances for geometry optimization. Corresponding to the method and basis set level of the TURBOMOLE runs, COSMOTherm used the parameter file BP_TZVP_C21_0111.ctd, which contains the parameters required to produce reliable, high-quality calculations of physicochemical data. The natural logarithm of the coefficient of activity was evaluated at room temperature and infinite dilution, taking the solute j as the pure solvent.[26]

The DPD mesoscopic simulations were performed by using the MS Mesocite software within simulation cells having dimensions of 10 × 10 × 10 DPD units (i.e., their volumes are $V_{\text{sim cell}} = 10^3\ r_c^3$) at the temperature $T = 1$ (in DPD units). According to the above-mentioned bead density ρ, the simulation cells contain a total of 3000 beads ($\equiv N_{\text{beads}}$), which were randomly allocated. We considered $N_{\text{total,DBT}} = N_{\text{total,MDR}} = 60$ total contents of the corresponding DBT and MDR beads. The remaining $N_{\text{beads}} - (N_{\text{total,DBT}} + N_{\text{total,MDR}}) = 2880$ beads are composed of a unique solvent, either HEX, DDC, DEC, or HEP.

The time-step size was 0.05 DPD units, and the simulations were performed during 1,000,000 time steps starting with random velocities; therefore, the total length time was 50,000 DPD units. The DPD unit $t_{\text{DPD unit}}$ for time is

$$t_{\text{DPD unit}} \equiv r_c\sqrt{\frac{m_b}{k_B T}} \tag{13}$$

where m_b is the mass of a bead, and the term $k_B T$ is the thermal energy. Herein, we take m_b as the average mass of DBT and MDR

$$m_b = \frac{1}{2}(m_{\text{DBT}} + m_{\text{MDR}}) \tag{14}$$

Likewise, for the evaluation of the non-bond DPD-force field terms by Mesocite, it was used, in addition to the cutoff distance r_c described at eq 8, a spline width of 0 and a buffer width of $r_c/2$. The spline width is the region below r_c in which non-bond interactions are forced to be splined from their full to null values; therefore, since the DPD force field vanishes itself when the center of two beads are separated by more than the distance r_c, the spline width is zero. The buffer width specifies the region from r_c where beads found there will be monitored because, during the dynamics simulation, they could be moved to less than r_c.

Mesocite runs also used a dissipation strength (γ) of 4.5 for the dissipative force ($\vec{F}_{D_{ij}}$), and a dissipation radius (r_D) of 1.0 times the cutoff distance r_c. As mentioned previously, the dissipative force $\vec{F}_{D_{ij}}$ is one of the three DPD forces acting on any pair of beads i and j; it is given by $\vec{F}_{D_{ij}} = -\gamma(1 - r_{ij}/r_D)(\dot{\vec{r}}_{ij}\cdot\hat{r}_{ij})\hat{r}_{ij}$ for $r_{ij} < r_D$, where $\dot{\vec{r}}_{ij} \equiv d\vec{r}_{ij}/dt$.

Finally, we monitor the adsorption of DBT beads by MDR ones through the radial distribution function $g_{ij}(r)$, which represents the probability of finding a bead j within a infinitesimal-dr-thickness spherical shell at a distance r from the bead i, normalized to the probability when the total number $N_{\text{total,j}}$ of beads j are distributed in the entire simulation cell with a homogeneous density $\rho_{\text{hom},j}$;[40] specifically:

$$g_{ij}(r) \equiv \left(\frac{dN_{ij}}{dV}\right)\Big|_r / \rho_{\text{hom},j} \tag{15}$$

where dN_{ij} is the number of beads j within the spherical shell's volume $dV = 4\pi r^2\ dr$ around a central bead i, and $\rho_{\text{hom,j}} \equiv N_{\text{total},j}/V_{\text{sim cell}}$. Due to its normalization, $g_{ij}(r)$ accomplishes the following limiting condition:

$$\lim_{r \gg r_c} g_{ij}(r) = 1 \tag{16}$$

That is, at large distances from a central bead i, the beads j occupy the space randomly under a probability uncorrelated with that of the central bead i.

The radial distribution function $g_{ij}(r)$ was calculated for each of the $N_{\text{total},i}$ beads of the species i and for all frames of the Mesocite DPD trajectory, which were written each 100 time steps; i.e., a $g_{ij}(r)$ graph is the result of the average performed over 6×10^5 neighborhoods configurations around central beads.

We can estimate the number $N_{\text{MDR,DBT}}(r_{\text{ads}})$ of DBT beads that can be adsorbed by a MDR bead within an adsorption radius r_{ads} by integrating $dN_{\text{MDR,DBT}}$ from eq 15:

$$N_{\text{MDR,DBT}}(r_{\text{ads}}) = 4\pi\rho_{\text{hom,DBT}}\int_0^{r_{\text{ads}}} g_{\text{MDR,DBT}}(r)r^2 dr \tag{17}$$

The adsorption radius r_{ads} can be insighted through a series of DFT geometry optimizations for DBT moved away at different distances from MDR until DBT was not attracted by MDR.

Finally, the efficiency η for adsorbing DBT by MDR can be measured as the fraction of the total $N_{\text{total,DBT}}$ of DBT beads found within r_{ads} for all MDR beads:

$$\eta = \frac{N_{\text{MDR,DBT}}(r_{\text{ads}}) \times N_{\text{total,MDR}}}{N_{\text{total,DBT}}} \tag{18}$$

For the particular case treated herein, in which $N_{\text{MDR,DBT}} = N_{\text{total,DBT}}$, the efficiency η is directly $N_{\text{MDR,DBT}}(r_{\text{ads}})$:

$$\eta = N_{\text{MDR,DBT}}(r_{\text{ads}}) \tag{19}$$

3. RESULTS AND DISCUSSION

The MDR representing the minimum model for the catalyst MoS_2 is thermodynamically stable, according to the negative value of its formation energy E_F (Table 1), i.e., the Mo_3S_6 cluster will not spontaneously decompose.

3.1. Quantum Adsorption. In the adsorption of thiophene by MDR, it is more feasible for electrons to be transferred from the thiophene to the catalyst since it requires only 0.424 eV, against 4.669 eV required for the opposite direction (Figure 3). From the topology of the HOMO of the

Table 1. Formation Energy E_F of MDR

atom or molecule	energy (Ha)
Mo	−3977.12748
S	−397.95486
Mo_3S_6	−14,320.30708
E_F	
Ha	kcal/mol
−1.1955	−750.16

https://doi.org/10.1021/acsomega.3c09613
ACS Omega 2024, 9, 45706−45718

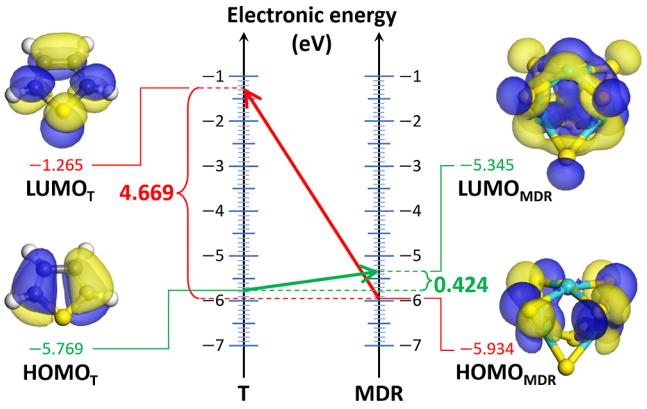

Figure 3. HOMO and LUMO of the thiophene (T) molecule (left) and the catalyst MDR (right). The blue and yellow colors of the isosurfaces denote positive and negative phases, respectively, of the molecular orbitals. The green and red arrows indicate the lowest and greatest difference energies among the crossed molecular orbitals, respectively.

thiophene and the LUMO of the catalyst, we have centered the thiophenic ring above a Mo atom of the Mo_3S_6 ring and oriented the molecular models in such a manner that their orbitals' lobes of the same colors (that is, having the same phase sign) are parallel to each other. After the DFT geometric optimization of this T:MDR complex, we built the DBT molecule by adding benzenic rings at the adsorbed thiophene, obtaining hence the complex DBT:MDR which afterward was optimized, as described in the quantum modeling section. The so-obtained molecular arrangement for the DBT:MDR complex (Figure 4a) is validated by the known fact that the sulfur-containing aromatic molecules prefer the adsorption on Mo atoms in a parallel orientation to the Mo-exposed edge, instead of perpendicular to the Mo-exposed edge or on the sulfur walls,[18] because the parallel configuration results in the more intense adsorption energy (Figure 4), facilitating to occur the C−S bond scission.[13]

The interaction energy ΔE in the complex DBT:MDR is −46.02 kcal/mol (Table 2), revealing that the DBT adsorption by MDR is exothermic because $\Delta E < 0$. This DBT adsorption through one MDR's Mo atom qualitatively agrees with the also-negative literature-reported interaction energy of −76.80 kcal/mol (−3.33 eV) obtained for DBT over a hexagonal MoS_2 cluster exposing a row of 3 Mo atoms instead,[18] which in addition to the DBT's thiophenic ring, also attract the benzenic rings, producing a more intense adsorption than in MDR.

Table 2. Interaction Energy ΔE Among DBT and MDR, Labeled as ΔE_a at Figure 4a[a]

molecular model	$E_{\text{non-dispersion}}$ (Ha)	$E_{\text{dispersion}}$ (Ha)	E (Ha)
DBT	−859.72935	−0.01459	−859.74394
MDR	−14,320.29335	−0.01373	−14,320.30708
DBT:MDR	−15,180.07596	−0.04841	−15,180.12436

		ΔE			
$\Delta E_{\text{non-dispersion}}$ (Ha)	$\Delta E_{\text{dispersion}}$ (Ha)	Ha	kcal/mol	D_{chem} (%)	D_{phys} (%)
−0.05325	−0.02008	−0.07334	−46.02	72.6	27.4

[a]Also reported are the non-dispersion $\Delta E_{\text{non-dispersion}}$ and dispersion $\Delta E_{\text{dispersion}}$ contributions, and the degrees of chemisorption D_{chem} and physisorption D_{phys}.

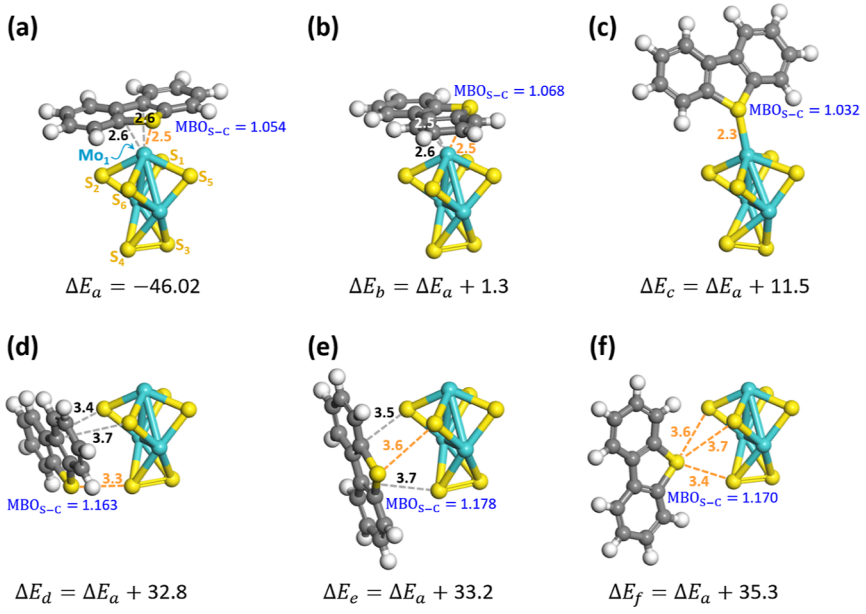

Figure 4. Different configurations for the adsorption of DBT over the MDR catalyst: DBT's plane parallel (a, b) and perpendicular (c) to a MDR's Mo edge; DBT's plane parallel (d, e) and perpendicular (f) to a MDR's sulfur wall. Below each i-th adsorption configuration ($i = a, b, ..., f$) it is shown the interaction energy ΔE_i (in kcal/mol) among DBT and MDR expressed in terms of that for $i = a$, whose configuration was obtained through the criterium of comparing the crossed HOMOs and LUMOs (Figure 3), and its interaction-energy value is detailed at Table 2. The coordination bonds of some DBT's atoms (S, C_6, and C_7, Figure 1a) binding MDR are shown by dashed lines, together with their bond lengths (in Å). As a reference for the orientation of MDR, some atoms' labels defined in Figure 1c are shown in (a). Blue labels display the Mayer-bond-orders (MBO_{S-C}) averaged over the bonds the DBT's S atom forms with its two neighboring atoms C_1 and C_{12} (shown at Figure 1a). Note that in general, the interaction energy weakens with the distance between the DBT's center and MDR, as expected.

https://doi.org/10.1021/acsomega.3c09613
ACS Omega 2024, 9, 45706−45718

Likewise, the DBT adsorption is a spontaneous process because there are not any barrier energies to overcome for DBT landing on the MDR (Figure 5); this means that once

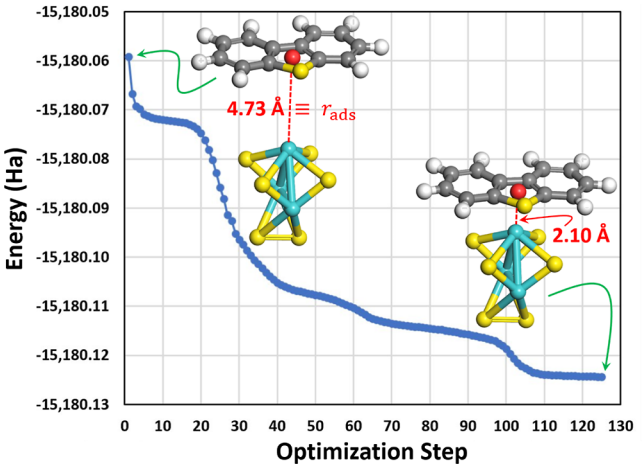

Figure 5. Energy evolution of the DBT adsorption by MDR starting at the greatest distance where DBT can be attracted from, labeled as r_{ads}. The symmetry center of DBT from which it is measured the DBT distance to MDR is indicated through a red ball.

DBT feels an attraction from the MDR at a certain distance r_{ads}, it will most likely be adsorbed. It is worth highlighting that the DBT adsorption is mainly chemisorption, although the physisorption character has a non-negligible presence (Table 2).

Testing other different configurations for the DBT adsorption (Figure 4b to f) confirms the strongest adsorption is that shown in Figure 4a, indicating the criterium based on crossed HOMOs and LUMOs is feasible to quickly obtain both the best adsorption site and the orientation on it of the adsorbed DBT. In general, the different adsorption configurations reveal, as is mentioned above, that the Mo edges are more reactive than the S walls (Figure 4). Although the interaction energy in the configuration shown in Figure 4f has the greatest deviation from that shown in Figure 4a, it also results from spontaneous and exothermic adsorption.

The net charge difference of DBT after its most stable adsorption is $\Delta q_{DBT} = +0.190\ e$ (Table 3); this confirms that there is an electronic transference from DBT to MDR, as insighted both from the above HOMO-LUMO analysis (Figure 3) and the chemisorption character (Table 2). In this process, the population of electrons on the DBT's carbon atoms C_1 and C_{12} linked to sulfur is increased ($\Delta q_{C_1} = \Delta q_{C_{12}} = -0.139\ e$), as well as on the MDR's molybdenum atom Mo_1 ($\Delta q_{Mo_1} = -0.085\ e$). This means an electronic bridge is formed connecting these DBT's carbon atoms with the MDR's Mo_1, through which the charge $\Delta q_{MDR} = -0.189\ e$ is received by MDR (Table 3).

From Table 3, it can be seen that it is accomplished the following relation below:

$$\frac{1}{2}\left(\Delta q_S + \overbrace{\Delta q_{C_2} + \Delta q_{C_6}}^{\text{transferred to } C_1} + \overbrace{\Delta q_{C_7} + \Delta q_{C_{11}}}^{\text{transferred to } C_{12}}\right) = 0.115\ e \approx -\Delta q_{C_1},\ -\Delta q_{C_{12}} \quad (20)$$

Table 3. Atomic Charges Before and After Adsorption of DBT Over MDR, Shown at Figure 4a

atom	charge (in e): before adsorption (q_{before})	charge (in e): after adsorption (q_{after})	difference of charges (Δq, in e)
		DBT	
S	−0.195	−0.064	0.131
C_1	−0.029	−0.110	−0.139
C_2	−0.095	−0.050	0.045
C_3	−0.114	−0.102	0.012
C_4	−0.109	−0.094	0.015
C_5	−0.122	−0.098	0.024
C_6	0.086	0.094	0.008
C_7	0.088	0.087	−0.001
C_8	−0.123	−0.097	0.026
C_9	−0.110	−0.095	0.015
C_{10}	−0.112	−0.100	0.012
C_{11}	−0.096	−0.050	0.046
C_{12}	0.030	−0.109	−0.139
H_1	0.110	0.133	0.023
H_2	0.107	0.123	0.016
H_3	0.105	0.121	0.016
H_4	0.099	0.111	0.012
H_5	0.099	0.111	0.012
H_6	0.105	0.121	0.016
H_7	0.107	0.123	0.016
H_8	0.110	0.134	0.024
total DBT difference charge Δq_{DBT}			0.190
		MDR	
Mo_1	0.537	0.452	−0.085
S_1	−0.269	−0.334	−0.065
S_2	−0.269	−0.304	−0.035
Mo_2	0.538	0.596	0.058
S_3	−0.269	−0.277	−0.008
S_4	−0.269	−0.239	0.030
Mo_3	0.538	0.605	0.067
S_5	−0.269	−0.359	−0.090
S_6	−0.269	−0.330	−0.061
total MDR difference charge Δq_{MDR}			−0.189

That is, the sources of electrons for both C_1 and C_{12} atoms are both the DBT's sulfur atom ($\Delta q_S = +0.131\ e$) and the carbon atoms to which they are bonded to, namely: C_2 ($\Delta q_{C_2} = +0.045\ e$) and C_6 ($\Delta q_{C_6} = +0.008\ e$) for C_1, as well as C_7 ($\Delta q_{C_7} = -0.001\ e$) and C_{11} ($\Delta q_{C_{11}} = +0.046\ e$) for C_{12}. Likewise, the other aromatic carbons from C_3 to C_9, along with all hydrogen atoms, are the source for the electrons transferred to the MDR, as their positive charge differences reveal (Table 3).

After the DBT adsorption, the S−C_1 and S−C_{12} bonds weaken, as indicated by their negative MBOs difference (Table 4); this effect is the key step for the HDS process to take place later where the S−C bonds are broken,[7] and validates therefore MDR as the simplest model for the MoS_2 catalyst. It is worthy to note that all C−H bonds have negative MBOs changes (Table 4), supporting the above finding that hydrogens and most of the aromatic carbons cede electrons, weakening as a consequence the C−H bonds.

For comparison, in the weakest DBT adsorptions (Figure 4d−f), the MBOs of the DBT's S−C bonds (1.163, 1.178, and

https://doi.org/10.1021/acsomega.3c09613
ACS Omega 2024, 9, 45706−45718

Table 4. Mayer Bond Orders Before and After of the Most Stable Adsorption of DBT by MDR (Figure 4a)

bond	Mayer bond order (MBO) before adsorption (MBO_{before})	Mayer bond order (MBO) after adsorption (MBO_{after})	change in the MBOs ($MBO_{after} - MBO_{before}$)
		DBT	
$S-C_1$	1.179	1.055	−0.124
$S-C_{12}$	1.179	1.055	−0.124
C_1-C_2	1.320	1.241	−0.079
C_1-C_6	1.207	1.068	−0.139
C_2-C_3	1.429	1.504	0.075
C_3-C_4	1.362	1.273	−0.089
C_4-S_5	1.450	1.508	0.058
C_5-C_6	1.314	1.258	−0.056
C_6-C_7	1.078	1.080	0.002
C_7-C_8	1.313	1.255	−0.058
C_8-C_9	1.450	1.511	0.061
C_9-C_{10}	1.361	1.271	−0.090
$C_{10}-C_{11}$	1.430	1.504	0.074
$C_{11}-C_{12}$	1.320	1.238	−0.082
$C_{12}-C_7$	1.207	1.062	−0.145
C_2-H_1	0.970	0.959	−0.011
C_3-H_2	0.972	0.969	−0.003
C_4-H_3	0.974	0.970	−0.004
C_5-H_4	0.973	0.972	−0.001
C_8-H_5	0.974	0.972	−0.002
C_9-H_6	0.974	0.970	−0.004
$C_{10}-H_7$	0.972	0.968	−0.004
$C_{11}-H_8$	0.970	0.958	−0.012
		MDR	
Mo_1-S_1	0.984	0.828	−0.156
Mo_1-S_2	0.984	0.825	−0.159
Mo_1-S_5	0.984	0.806	−0.178
Mo_1-S_6	0.984	0.803	−0.181
Mo_2-S_1	0.982	1.285	0.303
Mo_2-S_2	0.982	1.296	0.314
Mo_2-S_3	0.983	0.556	−0.427
Mo_2-S_4	0.983	0.487	−0.496
Mo_3-S_3	0.983	0.563	−0.420
Mo_3-S_4	0.983	0.508	−0.475
Mo_3-S_5	0.982	1.281	0.299
Mo_3-S_6	0.982	1.294	0.312
Mo_1-Mo_2	0.922	0.440	−0.482
Mo_1-Mo_3	0.925	0.455	−0.470
Mo_2-Mo_3	0.922	1.587	0.665
S_3-S_4	0.000	1.203	1.203
		DBT:MDR	
Mo_1-S	no bond	0.498	0.498
Mo_1-C_1	no bond	0.297	0.297
Mo_1-C_6	no bond	0.160	0.160
Mo_1-C_7	no bond	0.170	0.170
Mo_1-C_{12}	no bond	0.305	0.305

1.170, respectively) remain practically unchanged relative to those of the free DBT (1.179, Table 2). In contrast, the most evident effect for the weakening of the S−C bonds occurs in the adsorption configuration shown at Figure 4c (MBO: 1.032); this is due to it is formed a full covalent bond among the DBT's S and a catalyst's Mo, but its interaction energy lies 11.5 kcal/mol above that of the most stable configuration.

Interestingly, the MBOs reveal that in the free MDR, the Mo atoms are linked to each other through single bonds (MBO_{Mo-Mo} = 0.922, Table 4). However, after DBT adsorption, the bonds among the DBT-adsorbing Mo atom (Mo_1) and its neighbors Mo_2 and Mo_3 diminish (MBO differences: −0.482 and −0.470, respectively). Likewise, the bonds that Mo_1 has with each of its 4 neighboring sulfur atoms reduce too (their MBO differences vary between −0.181 and −0.156). This weakening of all bonds that Mo_1 has within MDR is due to after the MDR receives a net electronic transference from DBT, MDR in response also sends an electronic charge to DBT (Figure 6); that is, MDR accomplishes the well-known donation/backdonation of electron charges between an adsorbate and a catalytic surface, described at detail below, leading again to the validity of MDR as a catalyst model.

The remaining (carbon) atoms of the DBT's pentagonal aromatic ring bind Mo_1 too, but with lower bonds strengths: the bondings of C_1 and C_{12} to Mo_1 have MBOs ∼0.3, whereas C_6 and C_7 bind Mo_1 with MBOs around half of latter (Table 4). As discussed above, C_1 and C_{12} are responsible for the electronic transference from DBT; additionally, these MBOs result indicate that C_6 and C_7 also participate in this electronic transference, although within a minor grade.

In addition to the weakening of the $S-C_1$ and $S-C_{12}$ bonds, the strengths of the bonds C_1-C_6 and $C_{12}-C_7$ are lowered (Table 4). This is convenient for the HDS activity since carbons C_1 and C_{12}, further to having a trend for losing the sulfur atom, increase their reactivity for being saturated with hydrogen atoms.

The origin of the above charge transferences relies on the fact the MDR's Mo atoms are coordinatively unsaturated, that is, they are propense to form new bonds. Therefore, when DBT comes near MDR, Mo_1 donates electrons from its $4d_{xy}$ orbital (red-colored one in Figure 6a) to the DBT' S $3p_x$ orbital (red-colored one in Figure 6b). Once this electronic bridge is established, charges from the remainders MDR's Mo-$4d_{xy}$ and S-3*s* orbitals (pink-colored ones in Figure 6a) are donated onto DBT's C $2p_z$ orbitals (pink-colored ones in Figure 6b). This excess of charge received at the DBT aromatic rings induces electrons from C sp^2 orbitals (light-green-colored ones in Figure 6a) to be backdonated onto Mo-$4d_{z^2}$ and S-$3p_x$ orbitals (light-green-colored ones in Figure 6b) by using the DBT's S $3p_z$ orbital (dark-green colored one in Figure 6a) as a channel, whose electrons are also backdonated to the $4d_{yz}$ and $4d_{zx}$ Mo_1 orbitals (dark-green colored ones in Figure 6b). The net effect of these partial charge transferences is the changes in charges and in MBOs reported in Tables 3 and 4, respectively.

The partial density of states of the complex DBT:MDR (Figure 7) confirms the above-described electronic transference among DBT and MDR, since the initial electron-donating step done by Mo_1 is reflected by both the reduction of the *d*-peak height at the HOMO and the increasing number of *d*-peaks in the first unoccupied band of DBT:MDR (Figure 7b), relative to the same band of the free MDR (Figure 7c), as well as the corresponding rising of the *p*-peak just at the HOMO level of DBT:MDR complex due to occupation of the S $3p_x$ orbital (Figure 7b). Likewise, the back-donation from the S $3p_z$ orbital, which constitutes the HOMO of the free DBT (Figure 7a), lifts the *d*-peaks of Mo atoms below the HOMO of DBT:MDR at the time that strengthens the band of the first unoccupied band of *p* levels (Figure 7b). The consequent electronic cascade from *p* levels of the aromatic rings (*p* band

https://doi.org/10.1021/acsomega.3c09613
ACS Omega 2024, 9, 45706−45718

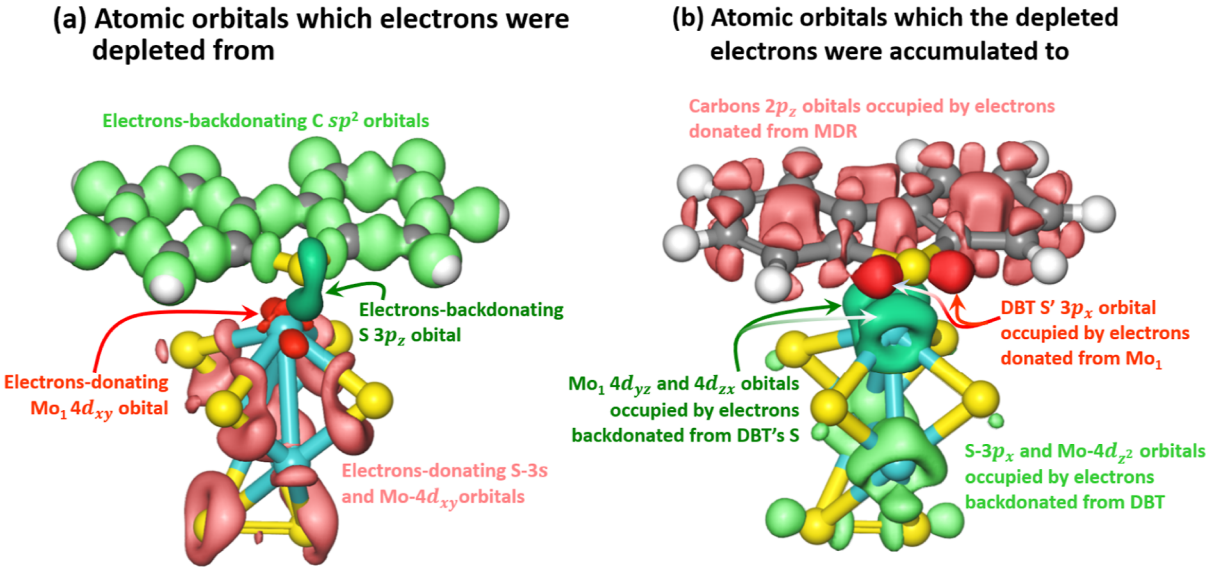

Figure 6. Isosurfaces of (a) positive and (b) negative charge density differences after the formation of the complex DBT:MDR. During the DBT adsorption process, electrons hop from atomic orbitals in (a) to atomic orbitals in (b) having the same color.

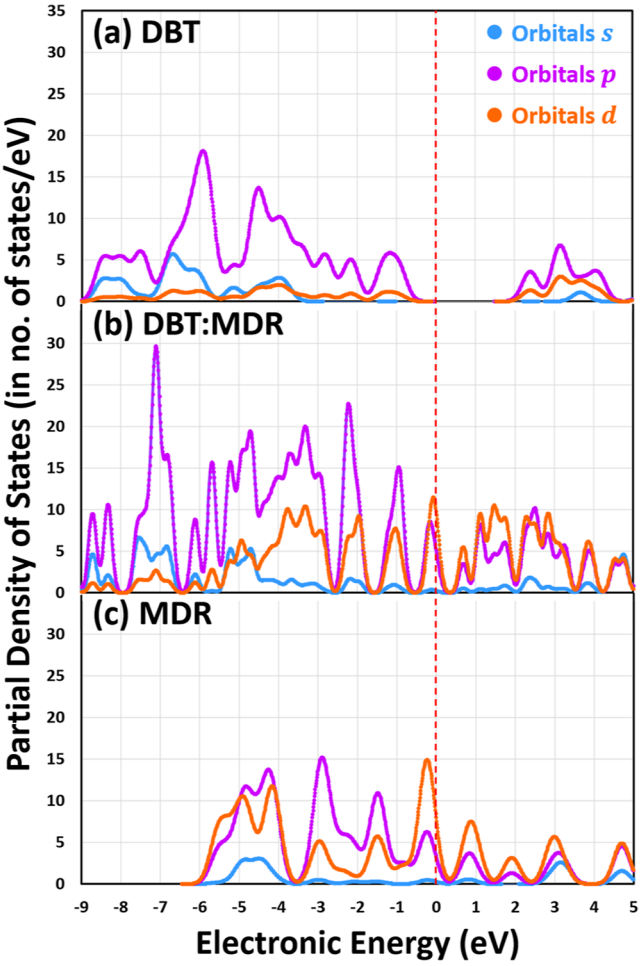

Figure 7. Partial density of states for (a) free DBT, (b) complex DBT:MDR, and (c) MDR. The vertical dashed red line indicates the position of the HOMO for DBT:MDR, which is taken as the zero for the electronic energies.

below the HOMO of free DBT, Figure 7a) is revealed by the elevation of the peaks of both the second unoccupied *p* band and the occupied *d* band of the complex DBT:MDR (Figure 7b). Finally, there is a notable unoccupied *d* band at the complex DBT:MDR because its electrons migrated to the occupied wide broad *p* band (Figure 7b).

It is worthy to highlight that the electronic clouds around DBT's S and MDR's Mo_1 (red and dark-green isosurfaces in Figure 6b, respectively) become very close to each other, leading to the strongest intermolecular bond, which has, however, a MBO weaker than that for a single covalent bond (0.498, Table 4). This implies that all bonds formed among DBT and MDR are noncovalent coordinate, i.e., the physisorption character, even being less than the chemisorption one (27.4 against 72.6%, respectively, Table 2), essentially preserves the DBT and MDR identities and, therefore, allows simulation of their intermolecular interaction by using classical descriptions, and specifically mesoscopic ones to model the collective adsorption.

3.2. Mesoscopic DPD Simulations. The SCDs projected on the COSMO surfaces reveal the polar character of DBT and MDR, as well as the nonpolar character of the alkylic hydrocarbons HEX, DDC, DEC, and HEP (Figure 8). However, the probabilistic measure of the distribution of these SCDs alongside the molecular surfaces reveals DBT has actually also a slight nonpolar character (Figure 9). These polar characters explain the fact that at room temperature the solubility of DBT in alkylic hydrocarbons is low, for example, ~2% mole fraction in *n*-octane, but increases by 1 order of magnitude with the temperature;[41] besides, explain the strong tendency of DBT to be absorbed by the MoS_2 catalyst, as it has been discussed above. Then, since the DPD interaction parameters we calculated herein are based on the quantum-determined σ profiles (Table 5), DPD simulations are expected to properly describe both the dissolution of DBT by the alkylic hydrocarbons and the attraction of DBT by MDR within these nonpolar solvents.

Most molecular-volume ratios v_{ij} have values around unity (Table 5), justifying the mesoscopic representation of the molecules through monobeads (Figure 2). In particular, from the molecular volumes for DBT and MDR (Table 5), the beads' volume has the value V_b = 227.955 Å^3 (eq 11); hence,

https://doi.org/10.1021/acsomega.3c09613
ACS Omega 2024, 9, 45706−45718

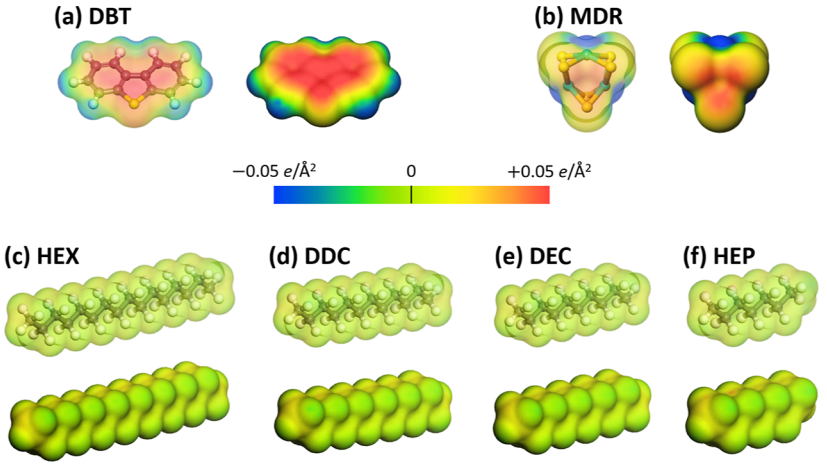

Figure 8. Transparent and opaque views of the COSMO surfaces within the infinite-dielectric continuum for (a) dibenzothiophene (DBT), (b) the molybdenum-disulfide ring (MDR), (c) *n*-hexadecane (HEX), (d) *n*-dodecane (DDC), (e) *n*-decane (DEC), and (f) *n*-heptane (HEP). The surface charge densities (SCDs) are projected onto the COSMO surfaces, where their values are represented according to the color code bar.

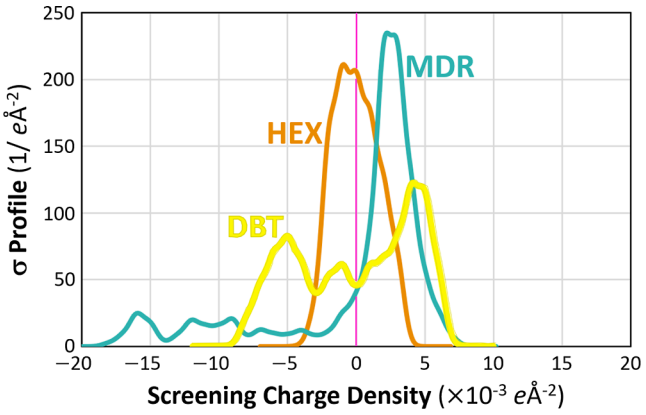

Figure 9. σ profiles $p(\sigma)$ for DBT, MDR, and HEX. It was not shown those for DDC, DEC, and HEP because they are very similar to that for HEX. The vertical pink line indicates the position of the null SCD σ. It is worthy to mention that each $p(\sigma)$ is normalized to unity, i.e., $\int_{-\infty}^{\infty} p(\sigma)\mathrm{d}\sigma = 1$. The single peak for HEX around zero σ indicates HEX is non polar. In contrast, both the right-shifted peak and the broad left band of MDR's $p(\sigma)$ reveal MDR is polar. DBT has mainly a polar character since its σ profile has peaks positioned at negative and positive SCD σ values, as well as a poor nonpolar character due to the small peak at around zero σ.

the cuttoff distance is r_c = 8.81 Å (eq 12) and the simulation-cells edges measure 88.10 Å. Likewise, by taking the hydrodesulfurization temperature around 300 °C, and using m_{DBT} = 184.256 and m_{MDR} = 480.180 g/mol, from eqs 14 and 13 we obtain the values m_b = 332.22 g/mol for the bead mass and $t_{DPD\ unit}$ = 7.36 ps for the DPD unit for time, i.e., the 0.05 × $t_{DPD\ unit}$ time-step size used in the Mesocite DPD runs is equivalent to 3.68 × 10^2 fs, and therefore the total time of the DPD simulations is 3.68 × 10^2 ns.

The DPD interaction parameter $a_{DBT,MDR}$ = 24.37 among DBT and MDR (Table 5) is less than the value of 25 for pure substances. Therefore, in the DPD framework the beads DBT and MDR have a trend to be together instead to keep as separate pure phases; that is, the DBT physisorption can occur. Likewise, MDR and the alkylic solvents have the greatest repulsive interactions (a_{ij} > 36, Table 5), which could lead to phase separation. Finally, DBT and the alkylic solvents have

Table 5. COSMO-Calculated Volumes of the Molecules Represented by Beads, and Calculation of the DPD Interaction Parameters a_{ij} From the Molecular-Volume Ratios V_{ij}, the Natural-Logarithm of the Infinite-Dilution Activity Coefficients $\ln(\gamma_{ij}^{\infty})$, and Flory-Huggins Interaction Parameters χ_{ij}^{∞}, According to Eqs 10 and 9

COSMO molecular volumes (in Å^3)					
DBT: 208.30	MDR: 247.61	HEX: 340.06	DDC: 257.03	DEC: 216.95	HEP: 160.65
bead *i*	bead *j*	v_{ij}	$\ln(\gamma_{ij}^{\infty})$	χ_{ij}^{∞}	a_{ij}
DBT	MDR	1.188	−0.192	−0.178	24.37
MDR	HEX	1.373	4.973	5.019	42.56
DBT	HEX	1.632	2.018	2.121	32.42
MDR	DDC	1.038	4.774	4.774	41.71
DBT	DDC	1.233	1.944	1.964	31.87
DEC	MDR	1.141	4.401	4.409	40.43
DBT	DEC	1.041	1.926	1.927	31.74
HEP	MDR	1.541	3.155	3.237	36.33
HEP	DBT	1.296	1.576	1.607	30.62

intermediate repulsive interactions (33 > a_{ij} > 30, Table 5), i.e., the process of DBT dilution by the alkylic solvents can be simulated by DPD runs.

After DPD simulations, it is confirmed that both DBT and MDR were kept in suspension in the solvents (Figure 10), that is, there is no phase separation. However, all radial distribution functions shown at Figure 11 have single peaks centered at $r < r_c$, revealing in particular that the MDR and DBT solute beads, when approach within the action range of the DPD forces, tend to form aggregates of either the same or different species. At this point, it is important to realize that the well-defined shapes of the radial-distribution-function graphics guarantee that thermal equilibrium has been reached during the long-time duration of the molecular-dynamics simulations (3.68 × 10^2 ns ≈ 0.4 μs, as mentioned above), over which each $g_{ij}(r)$ was averaged.

The height of the radial distribution functions indicates that, in any of the alkylic solvents, the MDR beads have a greater trend to approach each other (green curves in Figure 11) than DBT beads do (yellow curves in Figure 11); this phenomenon can be understood from the described molecular polarization: the MDR beads try notably to aggregate among them due to

https://doi.org/10.1021/acsomega.3c09613
ACS Omega 2024, 9, 45706−45718

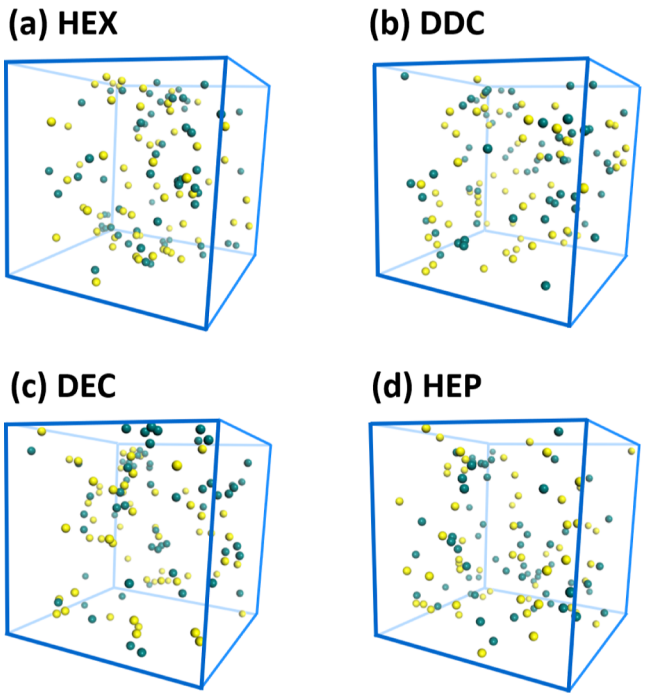

Figure 10. Perspective views of the DPD simulations at the runs' end for the mixing of DBT (yellow) and MDR (blue) beads, representing the dibenzothiophene molecule and the Mo_3S_6 ring, respectively, using (a) HEX (*n*-hexadecane), (b) DDC (*n*-dodecane), (c) DEC (*n*-decane), and (d) HEP (*n*-heptane) as solvents (not shown for the sake of a better visualization).

the strong polarization of the Mo_3S_6 ring; in contrast, the absence of polarization of the alkylic solvents (Figures 8 and 9) repels Mo_3S_6 rings, intensifying the attraction among latter. On the contrary, the weak neutral-SCD peak of dibenzothiophene suffices to produce lower heights of the DBT−DBT radial distribution function because its affinity with the single SCD peak of the alkylic solvents induces DBT to like somewhat the solvents, reducing then the DBT-DBT attraction.

Likewise, it is evident that the MDR-DBT radial distribution function (red curves in Figure 11) has intermediate values among those of the MDR-MDR and DBT-DBT beads pairs, which means that DBT beads prefer to be adsorbed by MDR beads rather than aggregate among themselves due the polar character of dibenzothiophene which is more intense than its nonpolar one (Figures 8 and 9).

The fact that, within any solvent, $g_{MDR,DBT}$ becomes constant around unity only for $r > r_c$ demonstrates that the adsorption of DBT by MDR does not occur by chance as when the beads are completely dispersed in the solvents; rather, the height of the $g_{MDR,DBT}$ peaks has values greater than unity increasing from ∼2 within HEP up to ∼3.5 within HEX.

The evident volcano form of the MDR-DBT radial distribution function is propitiated by the repulsion that the alkylic solvents exert on DBT, like as on MDR, due to the DBT's polarity, as can be seen from the position at $r \approx r_c$ of the maxima of the radial distribution function for DBT around any of the solvents beads (orange curves in Figure 11), strengthening therefore the attraction among DBT and MDR. In fact, it is very relevant to note that the top of the peaks for all $g_{MDR,DBT}(r)$ functions lies around the critical distance r_{ads} (Figures 11 and 5); this means that physisorption of DBT by MDR initiates at the greatest DBT density in the neighborhood of MDR, which happens about approximately a half r_c from MDR (Figure 11). This circumstance justifies calculating the efficiency η for the DBT adsorption (Eq. 19) through integrating $g_{MDR,DBT} \times r^2$ within the region $r \leq r_{ads}$, as proposed in eq 17.

The efficiency η of DBT adsorption by MDR goes with the molecular size of the solvent (Figure 12); i.e., for the solvents considered herein, η is lowest (6.68%) within *n*-heptane and highest (11.17%) within *n*-hexadecane. This is an entropic effect, since solvents' small molecular size allows DBT and MDR to access more spatial regions than big one does,

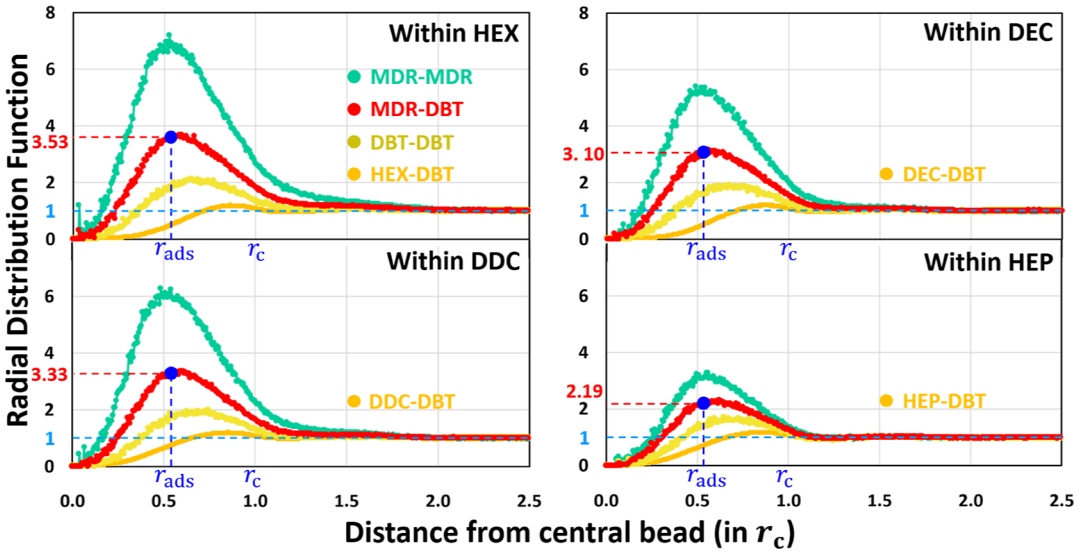

Figure 11. Radial distribution function $g_{ij}(r)$ for pairs of beads MDR-MDR, MDR-DBT, and DBT-DBT, within the solvents HEX, DDC, DEC, and HEP, for which it is also shown the $g_{ij}(r)$ they form with DBT. The vertical dashed dark-blue lines identify the position of the maximum distance r_{ads} in DPD units (= 4.73 Å/8.81 Å = 0.537) at which DBT will start to be adsorbed by MDR (Figure 5), whereas the horizontal dashed red lines indicate the value of $g_{MDR,DBT}(r)$ evaluated at $r = r_{ads}$. The horizontal dashed light blue lines indicate the unity value of $g_{ij}(r)$, corresponding to the case of beads completely dispersed in the solvents.

https://doi.org/10.1021/acsomega.3c09613
ACS Omega 2024, 9, 45706−45718

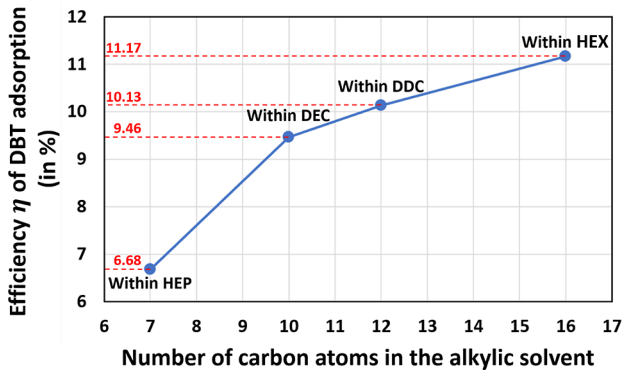

Figure 12. Efficiency η for the adsorption of DBT by MDR as a function of the length of the alkylic chain of the solvent.

inhibiting the probabilities for DBT to be found by MDR, as it is shown by the reducing of the $g_{MDR,DBT}(r)$ tops from 3.53 down to 2.19 when going from *n*-hexadecane to *n*-heptane (Figure 11).

4. CONCLUSIONS

From the molecular models proposed as the sulfur-containing hydrocarbon and the nanocatalyst for hydrodesulfurization (HDS), that is, dibenzothiophene (DBT) and the hexagonal Mo_3S_6 ring (MDR), respectively, we confirm that the process by which the sulfur-containing hydrocarbon adheres to the catalyst is chemisorption through a molybdenum atom. However, DBT and the Mo atoms form at most semicovalent bonds; this means that although there is donation/back-donation of electrons among them, so weakening the C−S bonds as desired for the HDS treatment, DBT and MDR somewhat preserve their molecular identity; then, the preliminary step for HDS to occur, i.e., the DBT adsorption by MDR, can be investigated by means of classical approaches. Mesoscopic dissipative-particle-dynamics (DPD) simulations over an oleic solution of a mix of DBT and MDR show that the volumetric density of DBT around the MDR nanoparticles is maximum approximately at half the cutoff distance r_c of the interaction among DPD beads, which coincides with the critical distance r_{ads} for spontaneous quantum adsorption to occur. The efficiency of adsorption, measured as the fraction of the content of DBT beads lying within the distance of adsorption r_{ads} from MDR nanocatalysts, grows with the size of the alkane solvent because *n*-alkyl chains having larger lengths repel more intensely the polar molecules, strengthening the attraction among latter. Above results show that the mesoscopic methodology could be applied to design better HDS catalysts and to select appropriate solvents due to that a greater fraction of dissolved hydrocarbons susceptible to be adsorbed, identified through DPD simulations, could indicate a better catalytic performance.

AUTHOR INFORMATION

Corresponding Authors

Jaime Klapp − *Departamento de Física, Instituto Nacional de Investigaciones Nucleares, 52750 Ocoyoacac, Estado de México, Mexico;* orcid.org/0000-0003-1828-9183; Email: jaime.klapp@inin.gob.mx

Raúl Oviedo-Roa − *Instituto Mexicano del Petróleo, Gustavo A. Madero 07730 CDMX, Mexico;* orcid.org/0000-0001-6443-1203; Email: oviedor@imp.mx

Authors

Estela Mayoral − *Departamento de Física, Instituto Nacional de Investigaciones Nucleares, 52750 Ocoyoacac, Estado de México, Mexico*

Ivonne Judith Hernández-Hernández − *Departamento de Física, Instituto Nacional de Investigaciones Nucleares, 52750 Ocoyoacac, Estado de México, Mexico*

José-Manuel Martínez-Magadán − *Instituto Mexicano del Petróleo, Gustavo A. Madero 07730 CDMX, Mexico;* orcid.org/0000-0003-1152-6924

Carolina Zuriaga-Monroy − *Instituto Mexicano del Petróleo, Gustavo A. Madero 07730 CDMX, Mexico*

Miriam Ballesteros-Olvera − *Instituto Mexicano del Petróleo, Gustavo A. Madero 07730 CDMX, Mexico*

Complete contact information is available at: https://pubs.acs.org/10.1021/acsomega.3c09613

Notes

The authors declare no competing financial interest.

ACKNOWLEDGMENTS

This work has been supported under the ENERXICO Project by the Mexican CONACYT-SENER-Hidrocarburos Grant Agreement no. B-S-69926 and by the European Union Horizon 2020 programme, Grant Agreement no. 828947.

REFERENCES

(1) Martínez-Palou, R.; Reyes, J.; Cerón-Camacho, R.; Ramírez-de-Santiago, M.; Villanueva, D.; Vallejo, A. A.; Aburto, J. Study of the formation and breaking of extra-heavy-crude-oil-in-water emulsions—A proposed strategy for transporting extra heavy crude oils,. *Chem. Eng. Process.* **2015**, *98*, 112−122.

(2) Skartlien, R.; Simon, S.; Sjöblom, J. DPD Molecular Simulations of Asphaltene Adsorption on Hydrophilic Substrates: Effects of Polar Groups and Solubility,. *J. Dispers Sci. Technol.* **2016**, *37* (6), 866−883.

(3) Speight, J. G.; Long, R. B.; Trowbridge, T. D. Factors influencing the separation of asphaltenes from heavy petroleum feedstocks,. *Fuel* **1984**, *63* (5), 616−620.

(4) *Asphaltenes and asphalts, 1: Development in petroleum science*; Chilingarian, G. V., Yen, T. F., Eds.; Elsevier: Netherlands, 1994.

(5) *Asphaltenes and Asphalts 2 Development in petroleum science*; Chilingarian, G. V., Yen, T. F., Eds.; Elsevier, 2000.

(6) Zhao, L., Zhai, D., Zheng, H., Ji, J., Wang, L., Li, S., Yang, Q., Xu, C. *Molecular Modeling for Petroleum-Related Applications*; Springer, 2015; pp 121−177. .

(7) Borges, I.; Silva, A. M.; Aguiar, A. P.; Borges, L. E. P.; Santos, J. C. A.; Dias, M. H. C. Density functional theory molecular simulation of thiophene adsorption on MoS2 including microwave effects,. *J. Mol. Struct.: THEOCHEM* **2007**, *822* (1−3), 80−88.

(8) Groenzin, H.; Mullins, O. C. Asphaltene Molecular Size and Structure,. *J. Phys. Chem. A* **1999**, *103* (50), 11237−11245.

(9) Sheu, E. Y. Petroleum AsphalteneProperties, Characterization, and Issues,. *Energy Fuels* **2002**, *16* (1), 74−82.

(10) Pecoraro, T. Hydrodesulfurization catalysis by transition metal sulfides,. *J. Catal.* **1981**, *67* (2), 430−445.

(11) G. A., Somorjai; Yimin, L. *Introduction_to_Surface_Chemistry_and_Catalysis*, 2nd Ed., Wiley 2010.

(12) Zhang, S.-F.; Sun, L.; Xu, J.-B.; Wu, H.; Wen, H. Aggregate Structure in Heavy Crude Oil: Using a Dissipative Particle Dynamics Based Mesoscale Platform,. *Energy Fuels* **2010**, *24* (8), 4312−4326.

(13) Kumar, N.; Seminario, J. M. Computational Chemistry Analysis of Hydrodesulfurization Reactions Catalyzed by Molybdenum Disulfide Nanoparticles,. *J. Phys. Chem. C* **2015**, *119* (52), 29157−29170.

(14) Hinnemann, B.; Moses, P. G.; Nørskov, J. K. Recent density functional studies of hydrodesulfurization catalysts: insight into

https://doi.org/10.1021/acsomega.3c09613
ACS Omega 2024, 9, 45706−45718

structure and mechanism,. *J. Phys.: Condens. Matter* **2008**, *20* (6), 064236.
(15) Wang, T.; Shang, H.; Zhang, Q. Adsorption behavior of thiophene on MoS2 under a microwave electric field via DFT and MD studies,. *Chem. Eng. Sci.* **2020**, *228*, 115950.
(16) Salazar, N.; Rangarajan, S.; Rodríguez-Fernández, J.; Mavrikakis, M.; Lauritsen, J. V. Site-dependent reactivity of MoS2 nanoparticles in hydrodesulfurization of thiophene,. *Nat. Commun.* **2020**, *11* (1), 4369.
(17) Zheng, M.; Zhao, L.; Cao, L.; Zhang, C.; Gao, J.; Xu, C. Catalysis performance of nonpromoted and co-promoted MoS2 catalysts on a hydrodesulfurization reaction: A DFT study,. *Mol. Catal.* **2019**, *467*, 38−51.
(18) Yang, T.; Feng, J.; Liu, X.; Wang, Y.; Ge, H.; Cao, D.; Li, H.; Peng, Q.; Ramos, M.; Wen, X. D.; et al. A combined computational and experimental study of the adsorption of sulfur containing molecules on molybdenum disulfide nanoparticles,. *J. Mater. Res.* **2018**, *33* (21), 3589−3603.
(19) Zonnevylle, M. C.; Hoffmann, R.; Harris, S. Thiophene hydrodesulfurization on MoS2; Theoretical aspects,. *Surf. Sci.* **1988**, *199* (1−2), 320−360.
(20) Diez, R. P.; Jubert, A. H. A molecular orbital picture of thiophene hydrodesulfurization. Part 2. Thiophene adsorption,. *J. Mol. Catal.* **1993**, *83* (1−2), 219−235.
(21) Raybaud, P.; Hafner, J.; Kresse, G.; Toulhoat, H. Adsorption of Thiophene on the Catalytically Active Surface of MoS_2: An Ab Initio Local-Density-Functional Study. *Phys. Rev. Lett.* **1998**, *80* (7), 1481−1484.
(22) Abbasi, A.; Sardroodi, J. J. Adsorption of thiophene on n-doped TiO_2/MoS_2 nanocomposites investigated by van der Waals corrected Density Functional Theory. *Surf. Rev. Lett.* **2018**, *25* (01), 1850038.
(23) Abbasi, A.; Abdelrasoul, A.; Sardroodi, J. J. Adsorption of CO and NO molecules on Al, P and Si embedded MoS_2 nanosheets investigated by DFT calculations. *Adsorption* **2019**, *25*, 1001−1017.
(24) Abbasi, A.; Sardroodi, J. J. Investigation of the adsorption of ozone molecules on TiO2/WSe2 nanocomposites by DFT computations: Applications to gas sensor devices. *Appl. Surf. Sci.* **2018**, *436*, 27−41.
(25) Abbasi, A.; Sardroodi, J. J. A novel strategy for SOx removal by N-doped TiO2/WSe2 nanocomposite as a highly efficient molecule sensor investigated by van der Waals corrected DFT. *Comput. Theor. Chem.* **2017**, *1114*, 8−19.
(26) Oviedo-Roa, R.; Martínez-Magadán, J. M.; Muñoz-Colunga, A.; Gómez-Balderas, R.; Pons-Jiménez, M.; Zamudio-Rivera, L. S. Critical micelle concentration of an ammonium salt through DPD simulations using COSMO-RS-based interaction parameters,. *AIChE J.* **2013**, *59* (11), 4413−4423.
(27) Abbasi, A.; Khataee, A. Band gap tunability and structural stability of metal/nonmetal codoped group-IV tin nanotubes: Effect of spin-orbit coupling. *Phys. E* **2019**, *114*, 113644.
(28) Wilfred, C. D.; Kiat, C. F.; Man, Z.; Bustam, M. A.; Mutalib, M. I. M.; Phak, C. Z. Extraction of dibenzothiophene from dodecane using ionic liquids. *Fuel Process. Technol.* **2012**, *93*, 85−89.
(29) Accelrys Software Inc., 2012. http://accelrys.com.
(30) Perdew, J. P.; Burke, K.; Ernzerhof, M. Generalized Gradient Approximation Made Simple. *Phys. Rev. Lett.* **1996**, *77* (18), 3865−3868.
(31) Delley, B. An all-electron numerical method for solving the local density functional for polyatomic molecules,. *J. Chem. Phys.* **1990**, *92* (1), 508−517.
(32) Delley, B. Ground-State Enthalpies: Evaluation of Electronic Structure Approaches with Emphasis on the Density Functional Method,. *J. Phys. Chem. A* **2006**, *110* (50), 13632−13639.
(33) Ramírez-Pérez, J. F.; Cerón-Camacho, R.; Cisneros-Dévora, R.; Martínez-Magadán, J. M.; Servín-Nájera, A. G.; Soto-Castruita, E.; Oviedo-Roa, R.; Zamudio-Rivera, L. S. Quantum-chemistry-computing and experimental development of a new n-alkenyl amino propionic and imino di-propionic acids-based gum inhibitor for gasoline. *Materials Today Sustainability* **2024**, *27*, 100798.
(34) Hoogerbrugge, P. J.; Koelman, J. M. V. A. Simulating Microscopic Hydrodynamic Phenomena with Dissipative Particle Dynamics,. *Europhys. Lett.* **1992**, *19* (3), 155−160.
(35) Español, P.; Warren, P. Statistical Mechanics of Dissipative Particle Dynamics,. *Europhys. Lett.* **1995**, *30* (4), 191−196.
(36) Groot, R. D.; Warren, P. B. Dissipative particle dynamics: Bridging the gap between atomistic and mesoscopic simulation,. *J. Chem. Phys.* **1997**, *107* (11), 4423−4435.
(37) Klamt, A.; Schüürmann, G. COSMO: a new approach to dielectric screening in solvents with explicit expressions for the screening energy and its gradient,. *J. Chem. Soc., Perkin Trans.* **1993**, *2* (5), 799−805.
(38) Klamt, A.; Eckert, F. COSMO-RS: a novel and efficient method for the a priori prediction of thermophysical data of liquids,. *Fluid Phase Equilib.* **2000**, *172* (1), 43−72.
(39) Balasubramani, S. G.; Chen, G. P.; Coriani, S.; Diedenhofen, M.; Frank, M. S.; Franzke, Y. J.; Furche, F.; Grotjahn, R.; Harding, M. E.; Hättig, C.; et al. TURBOMOLE: Modular program suite for ab initio quantumchemical and condensed-matter simulations. *J. Chem. Phys.* **2020**, *152*, 184107.
(40) Fan, T.; Chen, L.; Xia, X.; Wu, Y.; Zhang, J.; Yin, K. L.; Liu, F.; Yan, Z. Dissipative Particle Dynamics Quantitative Simulation of the Formation Mechanism and Emulsification Driving Force of Deep Eutectic Solvent-Based Surfactant-Free and Water-Free Microemulsion. *Ind. Eng. Chem. Res.* **2021**, *60* (7), 3249−3258.
(41) Tao, B.; Li, X.; Yan, M.; Luo, W. Solubility of dibenzothiophene in nine organic solvents: Experimental measurement and thermodynamic modelling. *J. Chem. Thermodyn.* **2019**, *129*, 73−82.

https://doi.org/10.1021/acsomega.3c09613
ACS Omega 2024, 9, 45706−45718